ARTICLE OPEN

Check for updates

Degradation of thermal oxide film on pure titanium in an acidic environment containing fluoride

Liwei Wang[1], Mingtao Wang[1], Mingyuan Zhong[2], Xiaoqi Li[1] and Zhongyu Cui[2]✉

Electrochemical degradation behavior of thermally oxidized pure Ti in the fluoride-containing acidic environments was investigated. Compact TiO_2 oxides with acceptable hardness and superior corrosion resistance are formed through the thermal oxidation at 650 °C for 24 h. Corrosion of the oxidized Ti depends on the oxidation condition and fluoride content, resulting in the various interfacial structures at the oxide/solution and metal/solution interface. Degradation of the oxidized Ti consists of three stages during long-term immersion, while its critical fluoride concentration is increased by 1~2 orders of magnitude, attributed to the high stability of the TiO_2 thermal oxides.

npj Materials Degradation (2022)6:65 ; https://doi.org/10.1038/s41529-022-00275-9

INTRODUCTION

Lining materials inside the chimney of the thermal power plant suffers severe corrosion attacks due to the aggressive condensates that formed from polluted gases when the surrounding temperature falls below the dew point[1,2]. The flue gas consists of a certain amount of acidic constituents (mainly SO_2) with low temperature and high humidity, resulting in the formation of the acidic condensates in which sulfuric acid is the dominant agent with other species including chlorides, fluorides, and nitrates[3–7]. To overcome the corrosion failure that experienced by glass fiber reinforced plastics, acid-resistant brick, and some coatings in the chimney[3,8], titanium (Ti) is recommended as the candidate material of lining materials by the International Committee on Industrial Chimneys and has been employed in some thermal power plants. Commercial pure Ti exhibits superior corrosion resistance in the H_2SO_4 environment[7,9], which is the final base constituent of the condensates attached on the lining materials. The trace amount of chlorides and nitrates in the condensates show limited effect on the corrosion of Ti, while the fluoride ions can seriously deteriorate the corrosion resistance, attributed to the dissolution of TiO_2 to soluble complex and the direct exposure of the titanium matrix[10–12]. Moreover, the low content of fluorides in the condensates cannot be neglected because it always exceeds the threshold value that induces severe corrosion of Ti in the power plant[13–15]. Therefore, it is important to further improve the corrosion resistance of pure Ti and illuminate its adaptability in the fluoride-containing acidic environments.

Thermal oxidation is a relatively simple and economical method of modifying titanium and its alloys. This method is aimed to produce in situ ceramic coatings, in the form of highly crystalline rutile oxide film, which generates a thermal oxide layer with enhanced hardness, wear resistance, and corrosion resistance[16–20]. From the perspective of corrosion resistance, Kumar et al.[16,21] reported that thermally oxidized pure Ti and Ti6Al4V alloy possessed corrosion resistance superior to that of the untreated alloy in Ringer's solution. Birch et al.[22] demonstrated that thermally oxidized titanium exhibited higher corrosion resistance than that of the pickled, polished, and anodized treatments in synthetic seawater. In the acidic environments, Shankar et al.[17] also found the improved corrosion resistance in highly aggressive nitric acid condensates. Besides, the proper thermal oxidation temperature and time are also determined by the authors.

In the presence of fluoride, corrosion of Ti deviates from the characteristics in other acids because of the easy formation of the Ti fluorides[9,23,24], resulting in the deterioration of the thin passive film and direct dissolution of the fresh Ti surface when the critical fluoride concentration is exceeded[7,15]. Wang et al.[7] found that the film on Ti was converted from a compact film to dual-layer with a porous outer layer and a barrier-like inner layer by fluoride ion in H_2SO_4. Huang et al.[24] reported that increasing fluoride concentration decreased the TiO_2 film protectiveness and accelerated the charge transfer process. Kong et al.[25] demonstrated that variation of fluoride concentration alters the rate controlling step during corrosion of Ti in $HClO_4$. In addition, corrosion induced by fluoride is also related to the presence form of the fluoride-containing species as declared by Amrutha et al.[11] who concluded that HF_2^- was the key species controlling the electrochemical step and remaining HF affected the chemical dissolution step. Moreover, effect of fluoride is highly depended on the solution pH, which is mainly reflected by its intrinsic relationship with the critical fluoride concentration[23,26,27]. As for the oxidized Ti, there is not enough research about the effect of fluoride on the degradation behavior of the thermal oxide film. Mareci et al.[28] investigated the corrosion behavior of the oxidized ZrTi alloy for dental implant application and found that corrosion resistance in acidic fluoridated environment was enhanced using thermal oxidation, while the degradation process and mechanism of the thermal oxide was not explicitly interpreted.

In the present work, the microstructure and corrosion behavior of the thermally oxidized pure Ti under different conditions are characterized. The effects of the oxide formation condition and fluoride concentration on the interfacial structure and corrosion kinetics are discussed. The long-term degradation mechanism of the optimized oxide film in the acidic fluorides is illuminated and the critical fluoride concentration is determined.

[1]College of Mechanical and Electrical Engineering, Qingdao University, Qingdao 266071, China. [2]School of Materials Science and Engineering, Ocean University of China, Qingdao 266100, China. ✉email: cuizhongyu@ouc.edu.cn

RESULTS

Morphology of the oxide film

Figure 1 shows the surface morphologies of pure Ti after thermal oxidation for 2 h and 24 h. The original scratches can be clearly observed after oxidation at 500 °C, indicating that the oxide film is extreme thin and cannot be distinguished by SEM (Fig. 1a, b). Even so, the oxide layer does form as demonstrated by the EDS results and the oxygen content increases with extending oxidation time (Supplementary Fig. 1). When the temperature is increased to 650 °C, numerous nanoscale oxide particles (Fig. 1d) and some isolated microscale particles (Supplementary Fig. 2a) are generated after 2 h. The former may be oxide nuclei and it can be found on the entire surface. The EDS results reveal that the chemical composition of the oxide particles and oxide film is almost the same (Supplementary Fig. 2b–d). With prolonging the aging time to 24 h, the oxide nuclei grow and form dense oxide layer, covering the entire surface (Fig. 1e) and the O content increases (Supplementary Fig. 2f). At 800 °C, formation and agglomeration of the oxide nanoparticles occur faster and a continuous surface layer is detected after oxidation for 2 h (Fig. 1g). Further extending the oxidation time results in the spalling and cracking of the oxide layer, leaving a rough surface with distinct cavities and bumps (Fig. 1h). The uneven cavities are not observed on other samples, which suggested that the local spalling is the direct reason that responsible for it. It is attributed to the generation of internal stresses because of the large lattice mismatch and the non-negligible differences in thermal expansion coefficient and volume ratio between Ti oxides and pure Ti[20,29–31]. The oxide film is thin and the formation rate is not high enough under other conditions, so the local spalling does not occur at lower temperature or with insufficient aging time.

The inserted images in Fig. 1 shows the surface topographies observed by AFM. The linear profiles marked in the figures are given in Supplementary Fig. 3 (*supporting information*). At 500 °C, the original scratches can be observed, yielding a low surface roughness of 68 nm (Fig. 1b'). At 650 °C, the nano-scale Ti oxide crystals, which display a step-like structure depicting the growth of pyramidal crystals, are perceived. The orientation of the crystal faces is identical for the different oxides as manifested by the parallel profiles (Supplementary Fig. 3), suggesting that the oxide growth has favorable orientation[32]. At 800 °C, the size of the well-developed crystals increases to about 1 µm along with the increase of surface roughness from 132 nm at 650 °C to 287 nm. The formation of pyramidal crystals could be ascribed to the diffusion of cations along dislocation core and diffusion towards the ledges located on the side walls[17].

The cross-sectional morphologies of the oxide film formed at different temperatures are presented with the backscattered electron images (Fig. 1c, f, i). The constituents of the epoxy resin have the lowest atomic number and has been sprayed a thin gold layer. Therefore, the substrate, the oxide layer, and the epoxy resin can be distinguished without the charging effect. A thin and homogeneous oxide layer with a thickness of about 2 µm is generated at 500 °C. The film thickness attains 8 µm at 650 °C. Moreover, at this temperature, the film is uniform in thickness and almost without observable spallation or cracking (Fig. 1b). As the temperature is increased to 800 °C, the oxide film is thickened to 55 µm. Meanwhile, the stratification characteristics are observed with numerous cracks that parallel to the underlying substrate (Fig. 1c), revealing the poor adhesion of this film. This can be demonstrated by the gaps between the oxide film and the oxygen-diffusion layer generated in some parts of the oxide/matrix interface (not shown).

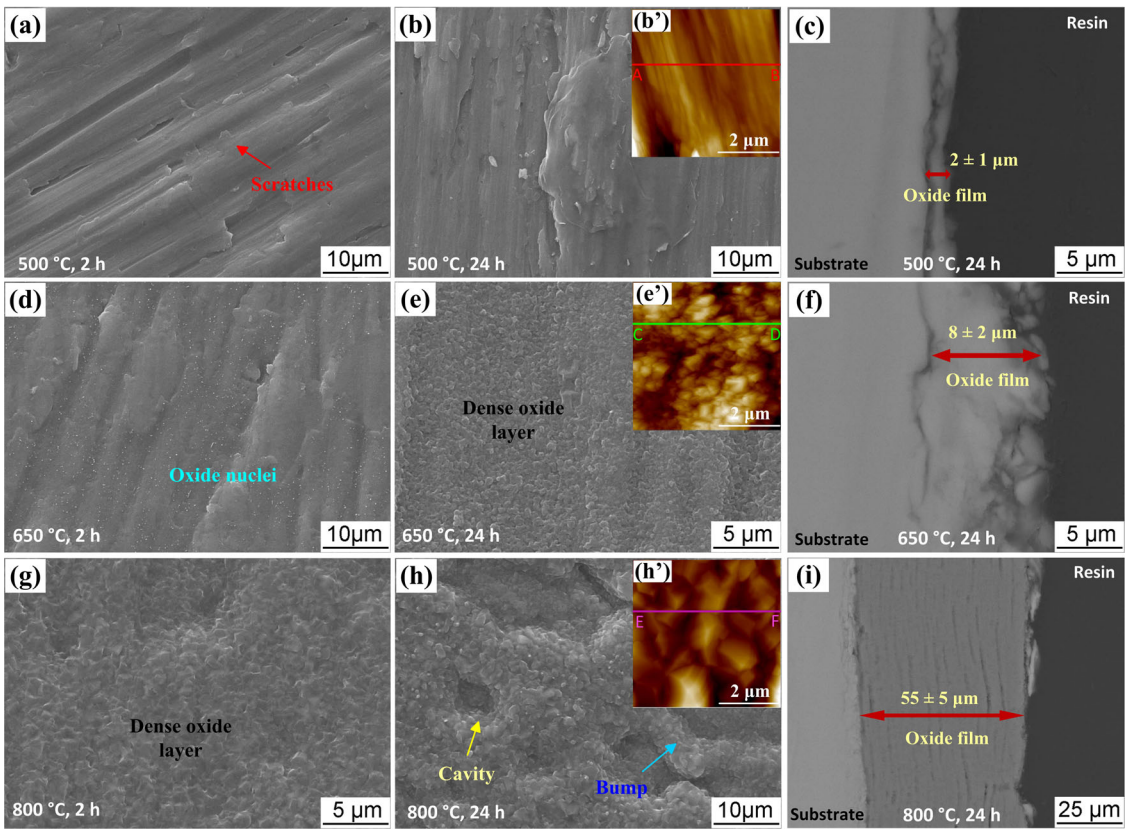

Fig. 1 Microstructure of the thermal oxide film formed on pure Ti. Surface morphologies (**a**, **b**, **d**, **e**, **g**, **h**), topographies (**b'**, **e'**, **h'**), and the cross-sectional morphologies (**c**, **f**, **i**) at 500 °C (**a**–**c**), 650 °C (**d**–**f**), and 800 °C (**g**–**i**) for 2 (**a**, **d**, **g**) and 24 h (**b**, **c**, **e**, **f**, **h**, **i**). The height ranges in **b'**, **h'**, and **e'** are −226 ~ 189 nm, −275 ~ 255 nm, and −399 ~ 499 nm, respectively.

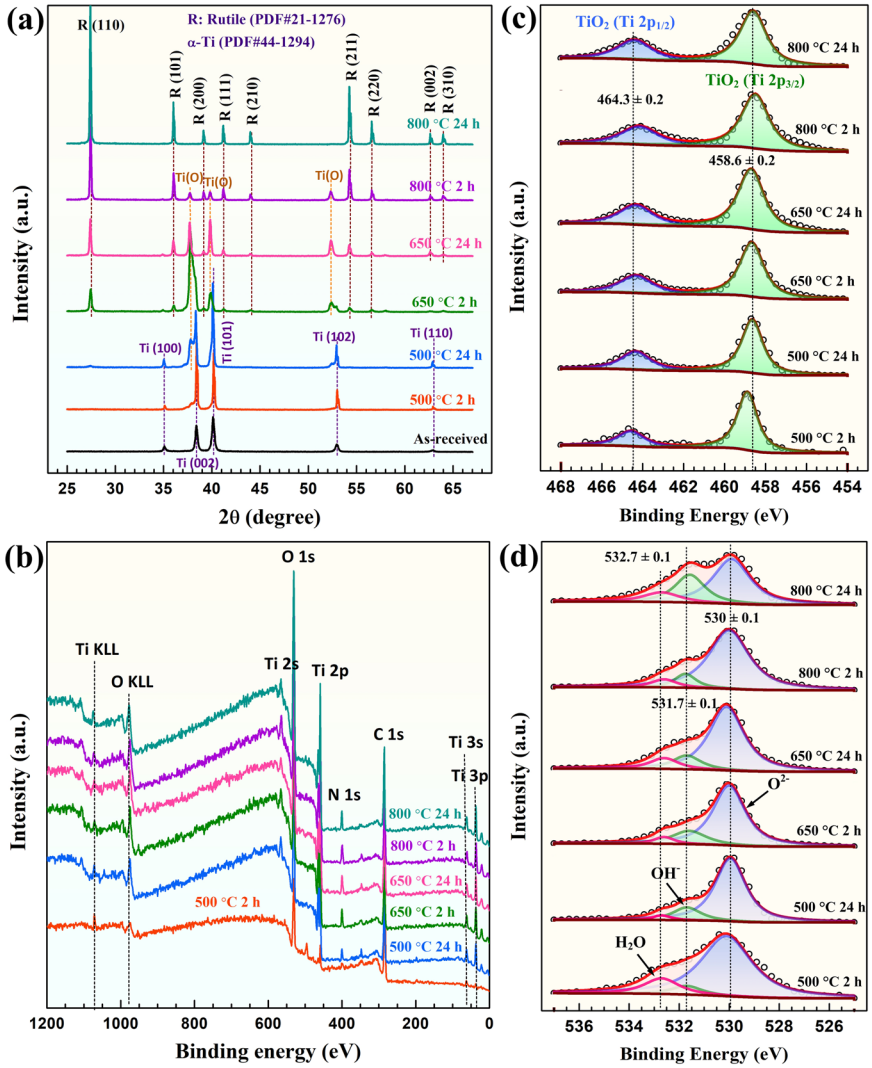

Fig. 2 XRD and XPS spectra of the thermal oxide film formed on pure Ti. XRD **a**, XPS survey spectra **b**, and the detailed spectra of Ti 2p **c** and O 1 s **d**.

Composition and hardness of the oxide film

Figure 2 displays the XRD and XPS spectra of the oxidized pure Ti at different temperatures for 2 and 24 h. As compared with the as-received Ti, widening of the Ti peaks and emergence of a shoulder pattern at lower diffraction angles are confirmed on the specimens treated at 500 °C. The presence of the shoulder corroborates the formation of oxygen diffused Ti (marked as Ti(O) in the XRD pattern) because the incorporation/diffusion of oxygen in α-Ti expands the lattice spacing[16,20,33]. Moreover, TiO_2 is not detected at 500 °C due to the thin oxide layer. As the oxidation temperature is increased to 650 °C, both TiO_2 (in the form of rutile) and Ti(O) are observed, with the former exhibiting more obvious peaks. At 800 °C, rutile phase dominates the surface oxide film and the Ti(O) phase cannot be detected after 24 h, implying that the rutile layer is too thick that the X-ray could not infiltrate up to the underlying Ti(O) layer. Considering the penetration depth of Cu-Kα radiation ranges from 10 to 20 μm, the presence and disappearance of α-Ti and Ti(O) peaks are consistent with the film thickness perceived by SEM.

The XPS survey spectra demonstrate that changing of oxidation temperature and time does not alter the film constituting elements. The element Ti, O, C, and N are detected on the oxidized samples (Fig. 2b). The high-resolution spectra of the Ti and O are given in Fig. 2c and d, respectively. The corresponding binding energy and full width at half maximum (FWHM) are listed in Supplementary Table 1 (*supporting information*). TiO_2 are confirmed as the constituent as indicated by the peak binding energy at 458.6 and 464.3 eV (Fig. 2c)[7,15]. Because the XPS can only trace the superficial layer within several nanometers, the composition beneath the surface layer is not detected, resulting in the presence of peaks only from TiO_2. Therefore, the changes of the oxidation states of the film from 500 to 800 °C cannot be confirmed by this technique. This is different from the passive film formed in electrolytes in which the different valances are verified because of the low film thickness. In addition, the peak broadens with increasing oxidation temperature and time as shown by the FHWM values. The O 1 s spectra are composed of three peaks from O^{2-} (530.0 eV), OH^- (531.7 eV), and H_2O (532.7 eV)[5,34]. The sample treated at 800 °C for 24 h shows the highest content of hydroxides, while that oxidized at 500 °C for 2 h exhibits the highest content of H_2O. Even so, the hydroxides, hydrates and/or adsorbed water only contribute low proportion of the surface film and the oxide dominates the surface film under all the conditions.

Figure 3 shows the micro-hardness of the oxide films formed under different conditions. It shows negligible changes after oxidation at 500 °C as compared to the as-received specimens, attributed to the low oxide layer thickness. After oxidation at 650 °C for 2 and 24 h, the samples exhibit higher hardness which is about 2.5 and 3 times that of the untreated sample. This parameter attains the maximum value at 800 °C for 2 h and then decreases with further extending aging time to 24 h at this temperature. During the thermal oxidation, diffusion of oxygen in the lattice increases the c/a ratio and strains and enhances the surface hardness in addition to the formation of hard oxide layer[16,20]. Prolonging oxidation time yields higher surface hardness due to the increased depth of the oxygen-diffusion zone. However, when the penetration of the indenter is restrained in the oxide layer, the spallation of this layer leads to a lower hardness (800 °C, 24 h).

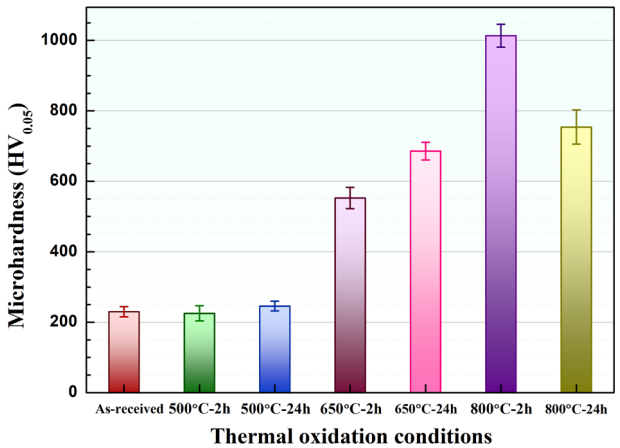

Fig. 3 Microhardness of the as-received and thermally oxidized pure Ti under different conditions. Error bars represent standard deviations of three independent titanium plates.

Electrochemical characterization of the oxide film

Figure 4 shows the OCP and polarization curves of the as-received and the oxidized pure Ti in the simulated condensates and the corresponding parameters. OCP of the as-received specimen stabilizes in the active potential range of Ti which is characteristic of surface activation. The sluggish positive shift of OCP with extending immersion time may be attributed to the formation of titanium hydrides[35]. After thermal oxidation, the OCP is significantly shifted to the noble values, locating within the potential region where TiO_2 is the stable phase (Fig. 4a). The positive or negative shift is discerned during the immersion process for the oxidized specimens, but all the OCPs become changeless at the end of the test except for that treated at 800 °C for 24 h. The quasi steady-state OCP values are illustrated by box charts in Fig. 4b, in which the boxes are roughly shifted upward with increasing oxidation temperature and time to 650 °C and 24 h, followed by a negative shift at 800 °C especially for 24 h.

As shown in the polarization curves, the bare Ti exhibits a conventional active-passive transition behavior with an apparent anodic peak (~−0.7 V_{SCE}) and a wide passivation zone (Fig. 4c). In the case of the oxidized samples, self-passivity occurs right from their respective corrosion potentials (E_{corr}), without the active

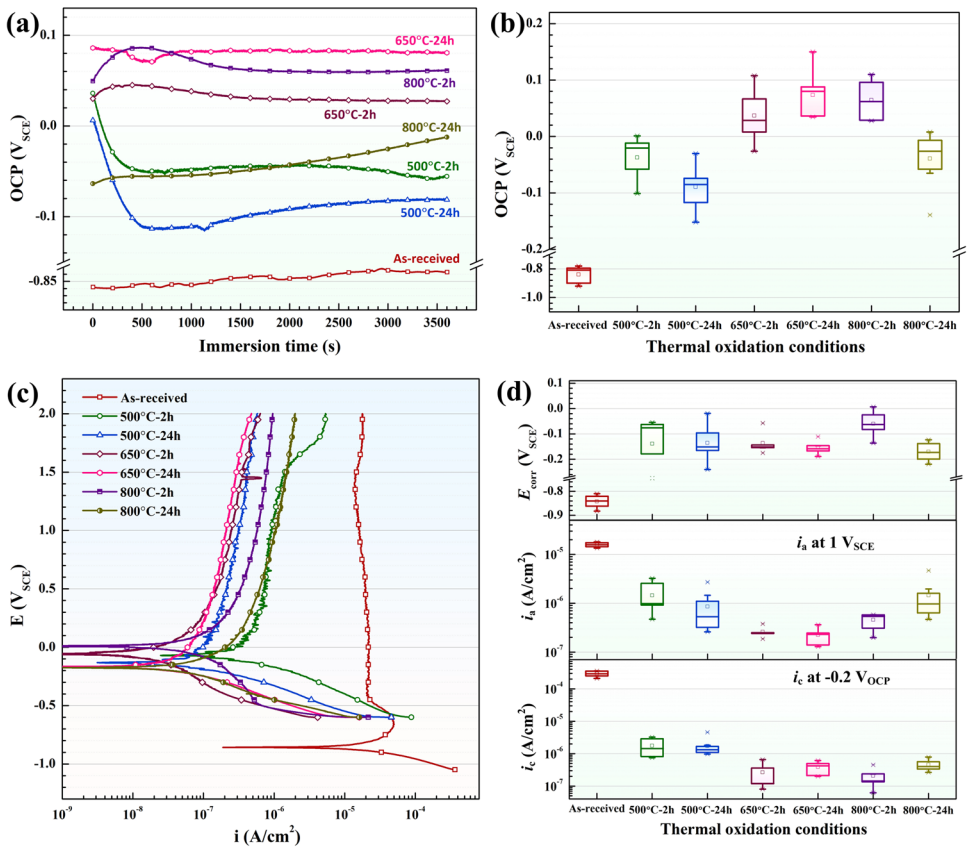

Fig. 4 OCP and potentiodynamic polarization of the as-received and thermally oxidized pure Ti in the simulated condensates. a open circuit potential, **b** the steady-state OCPs, **c** polarization curves and **d** the corrosion potential, the anodic current density at 1 V_{SCE}, and the cathodic current density at −0.2 $V_{vs.OCP}$ calculated from **c**. Error bars represent standard deviations of three independent samples from triplicate systems.

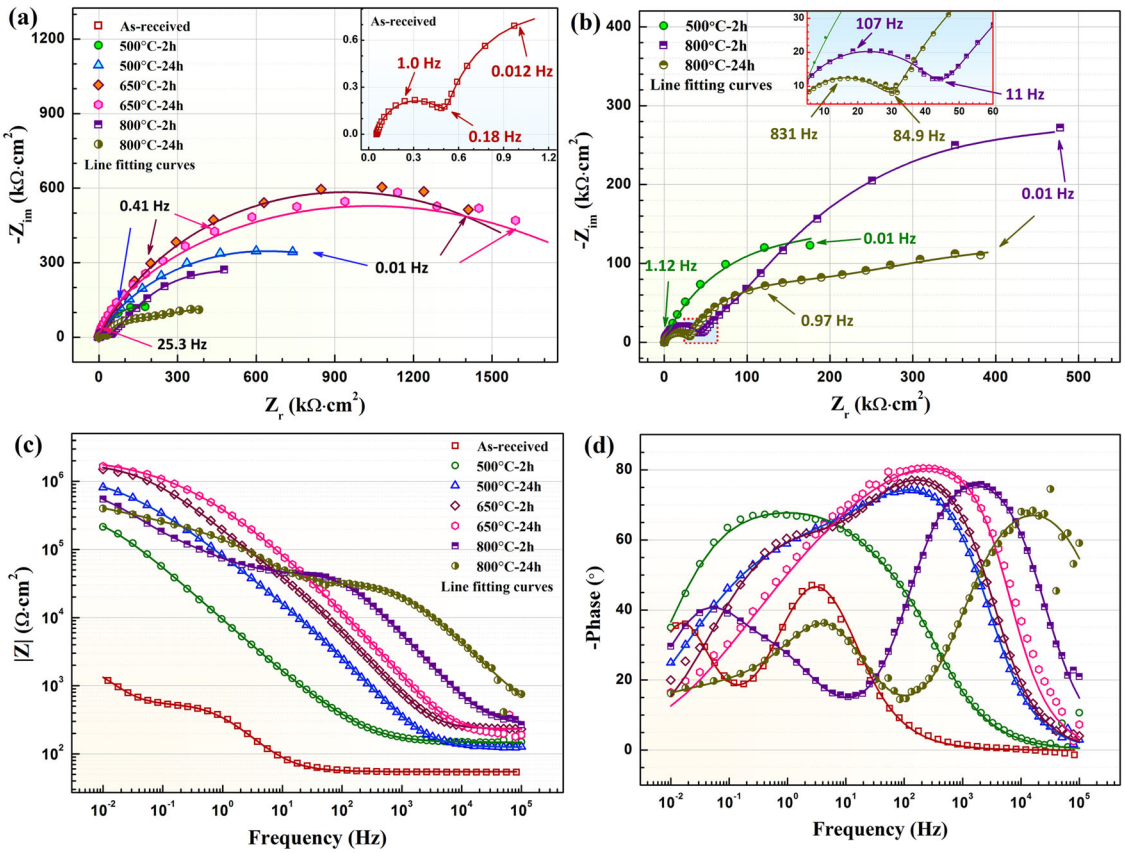

Fig. 5 EIS of the as-received and thermally oxidized pure Ti in the simulated condensates. Nyquist **a**, **b**, modulus **c**, and phase angle **d** diagrams of the EIS data.

dissolution region despite the existence of fluoride. Because the polarization curves of the oxidized Ti do not meet the strict prerequisites for the Tafel fitting[36,37], the following parameters including the E_{corr}, anodic current density at 1 V_{SCE} (i_a), and cathodic current density at −0.2 $V_{vs.OCP}$ (i_c) are compared (Fig. 4d). E_{corr} of bare Ti (−0.84 V_{SCE}) is located within the stable region of Ti^{2+}, while it is shifted positively to about −0.15 V_{SCE} after thermal oxidation because of the stable existence of TiO_2 layer. A weak dependence of the E_{corr} on the oxidation parameters is confirmed as indicated by the fluctuation of this potential with increasing oxidation temperature and time. When comparing the i_a values, anodic reactions are inhibited because of the barrier effect of the oxide scales. The specimen oxidized at 650 °C for 24 h exhibits the lowest i_a, which is two orders of magnitude lower than that of the bare Ti. The anodic current density increases as the oxidation temperature is increased to 800 °C, which is attributed to the poor interfacial properties of the film formed at this temperature. The mismatch between the lattice of the substrate and oxide film results in the local gaps at the film/substrate interface and thus facilitate the diffusion and contact of the aggressive electrolyte to the substrate and degrade the protective ability. As for the cathodic reactions, i_c presents three orders of magnitude drop from bare Ti to oxidized Ti at 650 and 800 °C, but the differences between these four samples are not impressive (Fig. 4d).

Figure 5 shows the EIS diagrams of the bare and oxidized pure Ti in the simulated condensates. The as-received specimen exhibits two well-defined capacitive arcs with low resistances (inserted image in Fig. 5a). After oxidation at 500 and 650 °C for 2 and 24 h, corrosion resistance is significantly improved as indicated by the high resistance values. The flattened capacitive arcs are difficult to separate but the Bode diagrams reveal the existence of two time constants (Fig. 5d). When the oxidation temperature is increased to 800 °C, barrier property of the oxide film is reduced as implied by the decrease of the capacitive arc diameter. Meanwhile, obvious high frequency capacitive arcs are identified within the frequency range higher than 11 Hz (2 h oxidation) and 84.9 Hz (24 h oxidation), suggesting the emergence of an additional process (inserted image in Fig. 5b). After that, the rather depressed capacitive loops at medium and low frequencies are traced, manifesting the existence of the other two time constants. Moreover, from the EIS results, the oxide film formed at 650 °C for 24 h possesses the highest modulus in this environment. The following experiments put the emphasis on the endurance capability of this layer in the acidic fluoridated environment.

Figure 6a, b show the polarization curves of pure and oxidized Ti in the simulated condensates with changing fluoride concentration. The pure Ti shows an apparent critical fluoride concentration, which can be identified between 0.001 and 0.002 M based on the transition from self-passivity to active dissolution at E_{corr}. In addition, the anodic passivation current (i_p) increases slightly with increasing fluoride concentration (Fig. 6a). As for the oxidized specimen, self-passivity with i_p lower than 1 μA/cm² still occurs when the fluoride concentration is 0.002 and 0.02 M. However, the E_{corr} drops to −0.5 V_{SCE} and i_p increases to values that are comparable with the pure Ti in the solution containing 0.2 M fluoride (Fig. 6b). An anodic peak is detected at ~−0.3 V_{SCE}, indicating the fast dissolution process of the Ti matrix or the sub-stochiometric oxide layer[25,38].

The EIS diagrams of the bare and oxidized Ti in H_2SO_4 with different concentrations of fluoride are given in Fig. 6c–f. When the fluoride concentration is lower than the critical value,

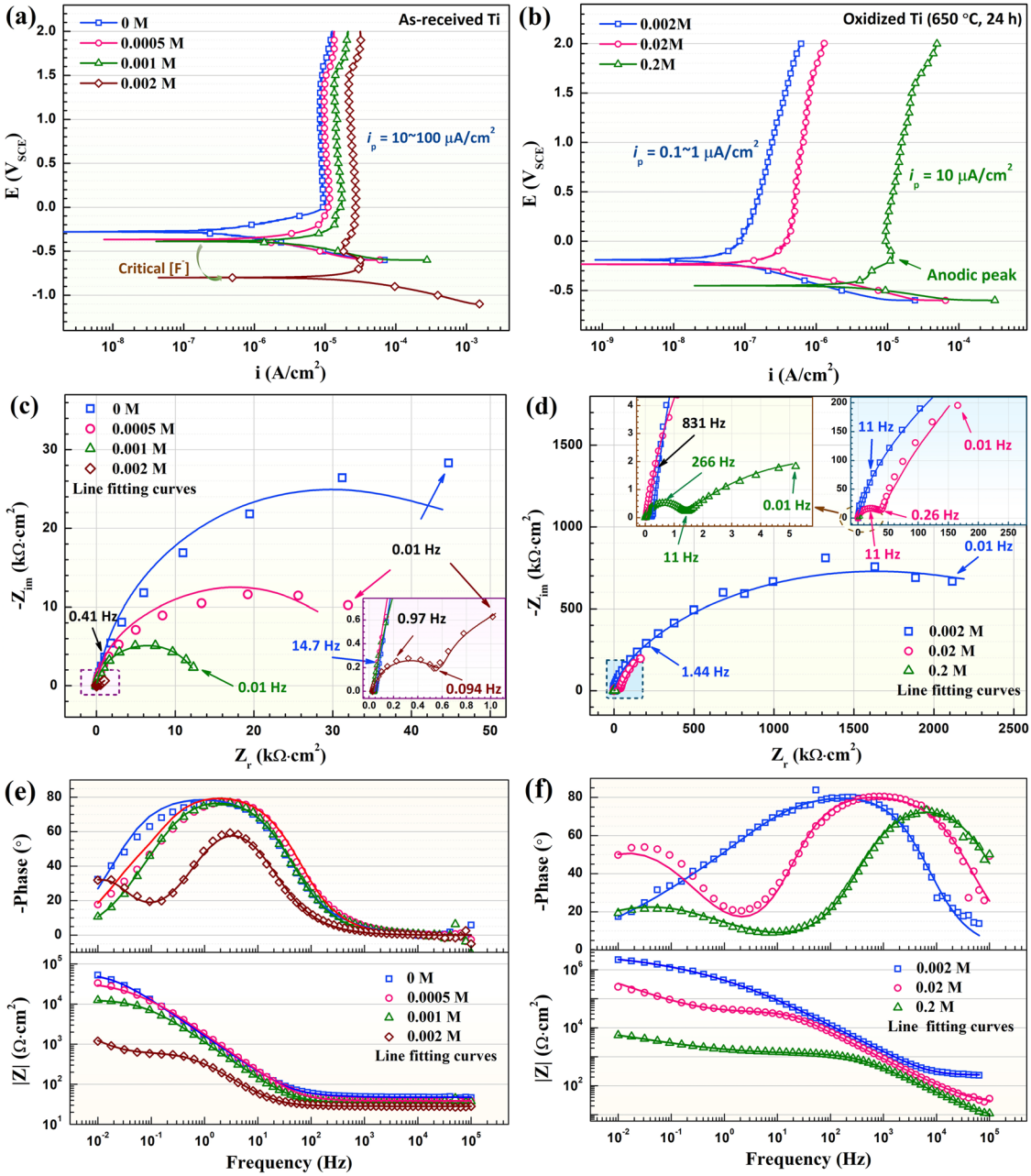

Fig. 6 Potentiodynamic polarization and EIS in fluoride-containing H_2SO_4 solutions (pH = 2). Polarization curves **a**, Nyquist **c** and Bode diagrams **e** of the as-received Ti and polarization curves **b**, Nyquist **d** and Bode diagrams **f** of the thermally oxidized Ti (at 650 °C for 24 h).

a capacitive loop which represents the compact barrier film is confirmed on pure Ti (Fig. 6c). Dissimilarly, two well-organized capacitive loops are observed at higher fluoride concentrations (inserted image in Fig. 6c, e). When the specimen is oxidized at 650 °C for 24 h, a depressed capacitive loop, which is originated from two processes, is obtained in the solution containing 0.002 M fluoride (Fig. 6f). As the fluoride concentration is increased to 0.02 and 0.2 M, the impedance values significantly decreases and the high-frequency capacitive loops are evidently distinguished (inserted images in Fig. 6d).

To examine the corrosion processes of the oxidized Ti in the acidic solutions containing fluoride, EIS was measured during the long-term immersion of the samples and the Nyquist and Bode diagrams are shown in Fig. 7 and Supplementary Fig. 4, respectively. Two well-arranged capacitive loops for the bare Ti are confirmed within the 72 h immersion (Fig. 7a), corresponding to systems exhibiting two time constants as revealed by the two maxima in the Bode-phase diagram (Supplementary Fig. 4b, *supporting information*). With further extending the immersion time, this phenomenon does not change except for some variations in the arc diameters. As for the thermally oxidized Ti, EIS characteristics change apparently with prolonging immersion time to 672 h. In the solution containing 0.002 M fluoride (Fig. 7b), the diameter of the impedance loop significantly decreases with increasing immersion time and a high-frequency capacitive loop is discerned at 72 h, which is similar to that obtained in Fig. 6d. Further extending the test, depressed capacitive arcs are detected. Even so, the modulus always keeps high values during the immersion test, implying the superior

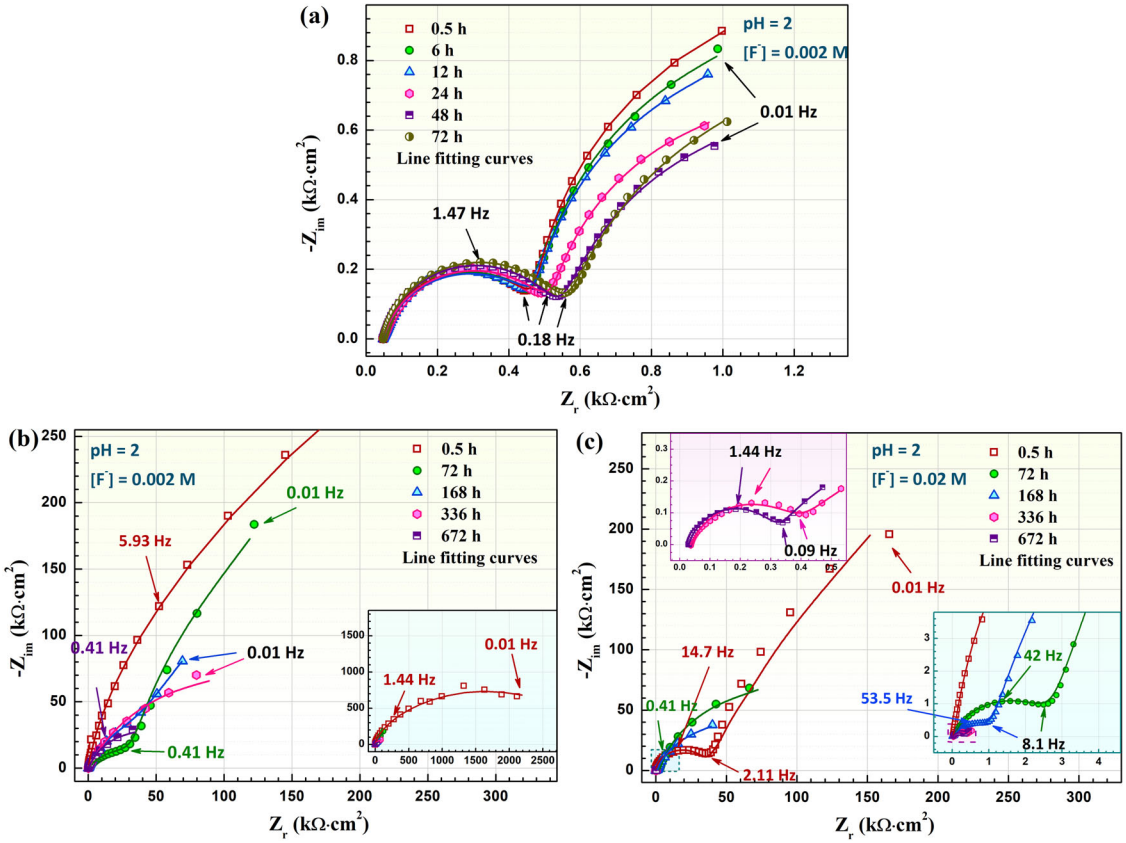

Fig. 7 EIS after immersion in the fluoride-containing H_2SO_4 solutions (pH = 2) for different time. Nyquist diagram of the as-received pure Ti after immersion in 0.002 M fluoride-containing solution for 72 h **a**, and Nyquist diagrams of the thermally oxidized pure Ti (at 650 °C for 24 h) during immersion in 0.002 M **b** and 0.02 M **c** fluoride-containing solutions for 672 h. The corresponding Bode diagrams can be found in Supplementary Fig. 4 in the supporting information.

corrosion resistance of the oxide film. As the fluoride concentration is added to 0.02 M (Fig. 7c), degradation of the oxide film is confirmed as supported by the decrease of the impedance modulus (Supplementary Fig. 4e). During immersion from 0.5 to 168 h, two capacitive arcs are detected and the diameters of these arcs contract with increasing immersion time. After that, remarkable changes are distinguished after immersion for 336 and 672 h, at which two well-defined capacitive loops are determined (inserted image in Fig. 7c). The diameter of these loops is only hundreds of ohms, suggesting the severe corrosion occurring on the sample surface. When comparing with the diagrams of pure Ti (Fig. 7a), it can be inferred that dissolution of bare Ti dominates the corrosion process during this period.

Corrosion morphology

Figure 8 shows the corrosion morphologies of the bare and oxidized Ti after immersion for 24 h. Slight uniform corrosion occurs on the bare Ti in the pH 2 solution with 0.002 M fluoride (Fig. 8a). As the solution pH drops to 0, remarkable active dissolution takes place, resulting in the generation of some cavities with sizes of 10–20 μm (Fig. 8c). By contrast, no apparent sign of corrosion attack on the surface of the oxidized Ti can be observed (Fig. 8b, d), signifying the improved corrosion resistance by the oxide film formed at 650 °C for 24 h.

DISCUSSION

Growth process of oxide film on titanium through thermal oxidation contains the following three steps including (i) the adsorption, dissolution, and diffusion of oxygen on titanium surface, (ii) the nucleation and growth of oxide scales on the metal surface, and (iii) transportation of anions, cations and electrons through the developing oxide film[39,40]. The oxidation temperature and time are the dominate factors that control the film performance. Lyapin et al.[39] reported that the high oxidation rates at high temperatures during the initial growth regime were attained by the electric field enhanced migration of cations across the oxide layer. In this case, considerable dissolution of oxygen into the titanium matrix occurs, contributing to the formation of rutile on the specimen surface (Fig. 2a). At low temperatures, however, the concentration-gradient-driven diffusion of cations and/or anions is negligible, resulting in the ending of the oxidation at a limiting thickness. Accordingly, non-stoichiometric oxide layer forms because of the concentration gradient of Ti-enrichment and O-deficiency within the oxide film that increases from the oxide surface towards the metal/oxide interface. In the present work, only rutile is confirmed and other Ti oxides (Ti_2O_3, TiO, etc.) are not detected by XRD (Fig. 2a). This is related to the oxidation temperature, time, and oxygen pressure. Padma et al.[41] built a theoretical model for the growth of Ti oxides by thermal oxidation and demonstrated that the oxides prepared for longer periods or at higher temperatures contained only rutile. Istrate et al.[42] reported that the percentage of rutile exceeded 99% when the oxidation time was longer than 2 h. Kofstad[43] conducted series of thermal oxidation experiments at different temperatures and oxygen partial pressures, the results confirmed that rutile was the only oxide phase at and above 10^{-3} torr O_2 and at temperatures below 1300 °C, while many kinds of Ti oxides (Ti_2O, TiO, Ti_2O_3, Ti_3O_5, TiO_2) could form at low pressures and high temperatures.

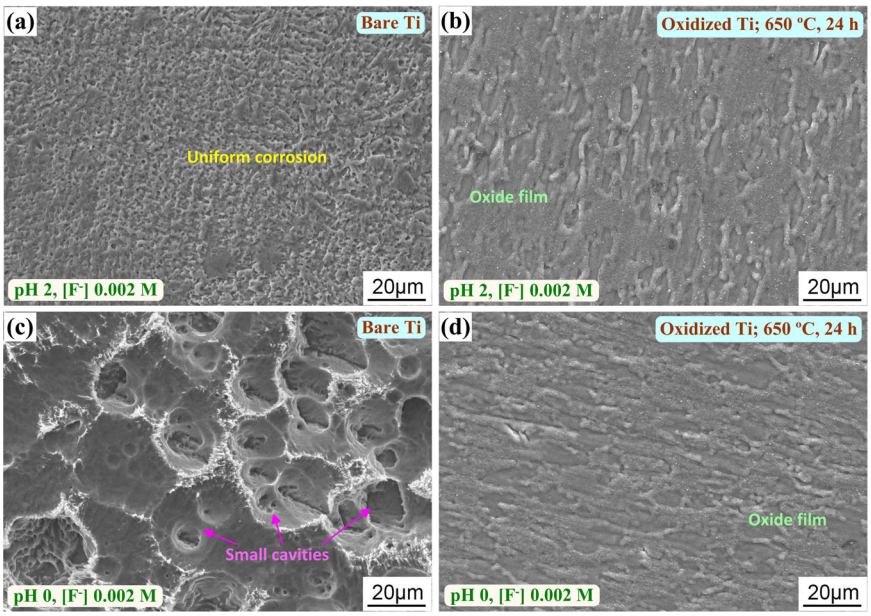

Fig. 8 Corrosion morphologies after immersion in the H_2SO_4 solutions containing 0.002 M fluoride for 24 h. As-received pure Ti in the solutions of pH 2 **a** and pH 0 **c**, and the thermally oxidized pure Ti (at 650 °C for 24 h) in the solutions of pH 2 **b** and pH 0 **d**.

Table 1. Summary of the reported optimal temperature and time for oxidation with good corrosion resistance in the literature.

Material	Oxidation temperature (°C)	Oxidation time	Electrolytes	Measurement approach	Optimum condition	Ref.
CP-Ti	25~700	1 h	Ringer's solution	PDP, EIS	400 °C, 1 h	38
CP-Ti	500~800	10, 30, 60 min	Synthetic seawater	PDP, EIS	700 °C, 30 min	22
CP-Ti	500~800	24 h	Ringer's solution	PDP, EIS	800 °C, 24 h	16
CP-Ti	650, 800	14 h	0.9% NaCl	PDP, EIS	650 °C, 14 h	45
CP-Ti	650	8, 16, 24, 48 h	Ringer's solution	PDP, EIS	650 °C, 48 h	21
Ti6Al4V	600, 650	12~60 h	5 mol/L HCl	Weight loss	600 °C, 24 h	46
Ti6Al4V	500~800	1 h	0.9% NaCl	PDP	600 °C, 1 h	20
Ti6Al4V	500~800	8, 16, 24, 48 h	Ringer's solution	PDP, EIS	650 °C, 24 h	44
Ti6Al4V	500, 700	1 h	Hank's solution	PDP	500 °C, 1 h	47
Ti6Al4V	600~800	4 h	Air	Tribological test	700 °C	18
Ti6Al4V	700	2~8 h	Air	Fretting test	700 °C, 4 h	48
Ti6Al4V	500, 650, 800	5~50 h	Air	Tribological test	650 °C, 25 h	49

Therefore, it can be deduced that the preferred formation of rutile in this work is attributed to the (i) the transformation of low-valence Ti oxides to rutile during long-duration oxidation, and (ii) the oxygen dissolution and rutile growth kinetics are much faster than that of lower valence oxides at the oxygen partial pressure in the ambient atmosphere. The rutile as the only oxide phase is also found on some Ti alloys[19,33,44], suggesting the chemical composition and microstructure are not the controlling factor.

Table 1 summarizes the reported optimal oxidation temperature and time for fabricating the thermal oxide film with high corrosion resistance in literature[16,18,20–22,38,44–49]. There is no agreement regarding the optimum parameter from a corrosion perspective. For example, Krishna et al.[38] found that the CP-Ti achieved the best corrosion resistance when oxidizing 1 h at 400 °C, which was the lowest temperature that reported in literature to the best of the author's knowledge. Kumar et al.[16] demonstrated that thermal oxidation of pure Ti at 800 °C for 24 h was a favorable surface treatment when oxidizing the specimen at 500, 650, and 800 °C. This value is the highest oxidation temperature that exhibits the best performance for titanium in the literature. Except this, all the optimal conditions in Table 1 belong to the moderate temperature ranging from 500 to 700 °C, at which the oxide film presents compact morphology, superior adhesion strength, and high hardness. Consequently, the oxide film possesses acceptable corrosion resistance in various kinds of environments including biological electrolytes[16,21,47], acidic solutions[46] and chloride medium[20,45], and superior wear resistance in air[18,48,49]. Even so, the applicability of the oxide film formed under different conditions in the presence of aggressive fluorides has not been investigated in detail. In the present work, the oxide film generated at 650 °C for 24 h has been proved to possess the best corrosion resistance in the acidic environment despite the existence of fluoride. Moreover, the protective ability can be preserved after long duration in the simulated condensates, suggesting that this thermal oxidation process is suitable for the fabrication of fluoride-resisting oxide layer on titanium.

Corrosion behavior of oxidized Ti depends on the oxide formation condition, fluoride concentration, and duration of the immersion. The degradation process and the controlling factors can be clearly presented by the EIS data. Figure 9 illustrates the

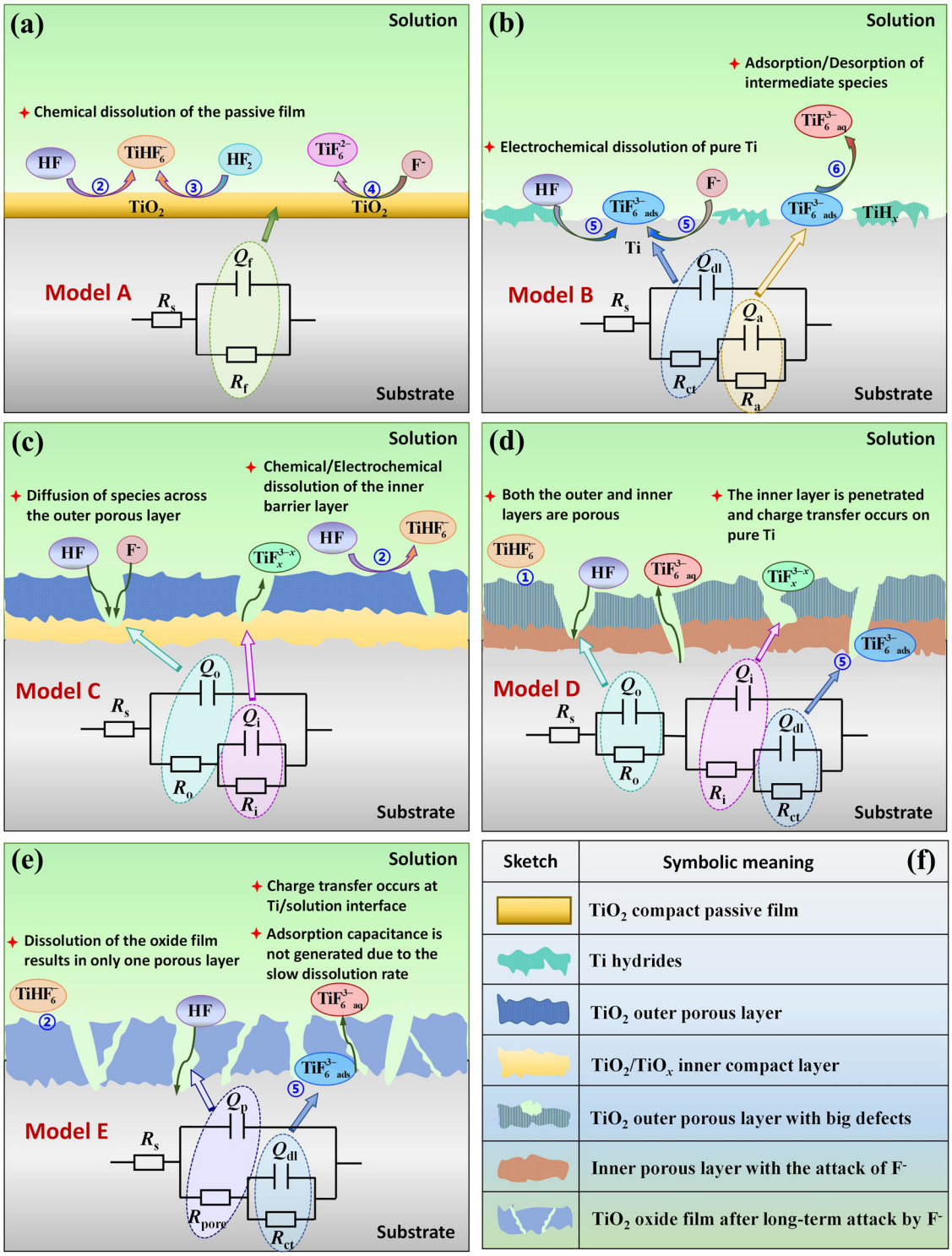

Fig. 9 Structural schematic and equivalent circuit diagram of EIS fitting. Schematic diagrams of the interfacial structures of the solution/oxide/metal interface and the corresponding equivalent circuits used in EIS fitting: **a** Model A, **b** Model B, **c** Model C, **d** Model D, **e** Model E, and descriptions of the graphical representations **f**. The reaction serial number coincides with that in the manuscript.

schematic diagrams of the interfacial structures of the bare and oxidized Ti in different environments and the corresponding equivalent circuits. The EIS data in Figs. 5–7 are fitted with the equivalent circuits and the fitting results are shown in Supplementary Table 2–5 (*supporting information*). The symbol Q is used to represent the constant phase element (CPE), which is converted to effective capacitance (C) according to the approach proposed by Hsu and Mansfeld[50] for the oxide layer (R is R_f) and Brug et al.[51] for the electrical double layer (R is R_s):

$$C = Q^{1/n} R^{(1-n)/n} \quad (1)$$

In fluoride-containing acidic environments, there exists a critical fluoride concentration above which Ti is significantly degraded. Conversely, the influence of fluoride on corrosion of

Ti is negligible. In the dilute H_2SO_4 (pH = 2), pure Ti exhibits spontaneous passivation with a passive current density lower than 30 μA·cm^{-2} as the fluoride concentration is not more than 0.001 M (Fig. 6a). Meanwhile, the Nyquist diagram presents a single capacitive arc which represents the response of the compact passive film at the metal/solution interface (Fig. 6c). Accordingly, the critical fluoride concentration has not been achieved and the system can be explained by the interface structure illustrated in Fig. 9a[24,52], in which the Q_f and R_f denote the capacitance and resistance of the surface film, respectively. In this case, a thin passive film composed of the outer TiO_2 and inner low-valence Ti oxide layer is formed on the specimen surface[34,53]. Three distinct fluoride-containing species including HF, HF_2^-, and F^- are existed in the acidic solution, with the HF as the dominant presence form[54]. The surface TiO_2 film dissolves with the following reactions[55,56]:

$$TiO_2 + 6HF \rightarrow TiHF_6^- + 2H_2O + H^+ \quad (2)$$

$$TiO_2 + 3HF_2^- + 2H^+ \rightarrow TiHF_6^- + 2H_2O \quad (3)$$

$$TiO_2 + 6F^- + 4H^+ \rightarrow TiF_6^{2-} + 2H_2O \quad (4)$$

The passive film is deteriorated intensely with increasing fluoride concentration, causing the decrease of the film resistance and increase of the film capacitance (Supplementary Table 2), which can be ascribed to the thinning and roughening of this film.

As the fluoride concentration exceeds the critical value, obvious drop of the impedance modulus occurs accompanied by the negative shift of the corrosion potential (Fig. 6a, e). The protective TiO_2 oxide no longer exists because of the abundant presence of fluoride, yielding a bare surface with severe electrochemical dissolution. In this case, corrosion of pure Ti consists of the following two successive processes including the charge transfer process and the adsorption/desorption of the intermediate species[11,15,25]:

$$Ti + 6HF \rightarrow TiF_{6\,ads}^{3-} + 6H^+ + 3e^- \text{ or } Ti + 6F^- \rightarrow TiF_{6\,ads}^{3-} + 3e^- \text{ First step} \quad (5)$$

$$TiF_{6\,ads}^{3-} \rightarrow TiF_{6\,aq}^{3-} \text{ Second step} \quad (6)$$

where $TiF_{6\,ads}^{3-}$ and $TiF_{6\,aq}^{3-}$ are the intermediate species adsorbed on Ti surface and dissolved into solution, respectively. According to our previous mathematical derivation[15] and the diagnosis criterion of the EIS[57], the two-step dissolution mechanism of Ti yields two capacitive loops. Therefore, the Model B displayed in Fig. 9b is used to fit the EIS data. In this model, Q_{dl} and R_{ct} represent the double electrode layer capacitance and the charge transfer resistance, respectively, which correspond to the high-frequency capacitive arc in Fig. 6c and Fig. 7a. The element Q_a and R_a express the adsorption capacitance and resistance, respectively. Considering the adsorption process belongs to the slow procedure during the electrochemical corrosion, this process contributes to the capacitive loop within the low frequency range[58]. The fitted parameters in Supplementary Table 4 with this model can be associated with the kinetic parameters of the two processes with the following equations:

$$\theta_{ss} = \frac{K_1}{K_1 + K_2} \quad (7)$$

$$\frac{1}{R_a C_a} = \frac{K_2}{\Gamma_0} \quad (8)$$

$$\left(\frac{1}{R_{ct}} + \frac{1}{R_a}\right)\frac{1}{C_a} = \frac{K_1}{\theta_{ss}\Gamma_0} \quad (9)$$

where K_1 and K_2 (mol·cm^{-2}·s^{-1}) are the apparent rate constants of the two steps given in Eqs. (5) and (6), respectively, θ_{ss} is the coverage fraction of the adsorbed species, and Γ_0 is the number of the available sites for adsorption (10^{-8} mol^cm^{-2})[59]. Figure 10 shows the calculated parameters of pure Ti during immersion for 72 h (EIS data from Fig. 7a). With extending exposure time, the capacitance and resistance of the two successive steps are relatively stable with some fluctuations within a limited range, suggesting that corrosion of pure Ti proceeds with a steady rate (Fig. 10a). The time constant ($\tau = CR$) of the adsorption process is two orders of magnitude higher than that of the charge transfer reactions, while its apparent rate constant (K_2) is obviously lower (Fig. 10b), implying that the chemical dissolution step is the rate controlling procedure during corrosion of pure Ti. This slow step creates surface adsorbed species which accumulate on the specimen surface, resulting in a high surface coverage (Fig. 10c).

From Figs. 4–5 and Supplementary Table 2, electrochemical response of the surface oxides is highly dependent on the oxidation condition. When the oxidation temperature is 500 and 650 °C, compact oxide layer is generated, obstructing fluoride to contact with the Ti substrate beneath it. In this case, the depressed capacitive loop characterizes the response of the dual-layer structure of the surface oxide consisting of a porous outer layer and a dense inner layer[24,38,60]. Consequently, the equivalent circuit model illustrated in Fig. 9c is used to interpret the film characteristics, in which the Q_o and R_o denote the capacitance and resistance (or pore resistance) of the outer layer and Q_i and R_i signify the capacitance and resistance of the inner layer[61–63]. According to Supplementary Table 2, the film resistance of the outer and inner layer increases with increasing oxidation temperature from 500 to 650 °C and prolonging oxidation time, indicating the promoted protectiveness of the oxide film. Meanwhile, the capacitance of the two layer decreases, attributed to the increase of film thickness and compactness. Both the film resistance and capacitance of the outer layer is 1~2 orders of magnitude lower than that of the inner layer, suggesting that the thin but compact inner dense layer contributes to the superior corrosion resistance. As the oxidation temperature is increased to 800 °C, a well-defined high-frequency capacitive loop is detected (Fig. 5). Considering the charge transfer reaction is the fast process during the corrosion, this loop can be ascribed to the electrochemical dissolution of Ti at the oxide/metal interface, where the oxide has been penetrated by the corrosive electrolytes[28,64]. The porous stratified oxide layer with cracks and gaps formed at this temperature, which provides diffusion routes for the fluoride, also supports this speculation (Fig. 1i). Even so, the available sites for the electrochemical dissolution of Ti substrate is limited, resulting in the low C_{dl} because of the low effective area[61,65,66] and the high film resistance in the orders of ~10^5 Ω·cm^2. Furthermore, the polarization resistance (R_p), which is the limit of the impedance at zero frequency, is calculated and listed in Supplementary Table 2. The oxide formed at 650 °C for 24 h exhibits the highest value and reveals the best protection ability.

The interfacial structure of the oxide film is altered with increasing fluoride concentration (Fig. 6d). The data obtained in the dilute solution containing 0.002 M fluoride is similar to that in Fig. 5a and can be interpreted with the Model C. However, only two well-distinguished capacitive loops can be identified when the fluoride concentration is increased to 0.02 and 0.2 M. In this case, the surface oxide layer is severely destroyed by HF and the outer and inner oxide layer cannot be discerned. The model illustrated in Fig. 9e is used to elucidate the EIS data in which the Q_p and R_{pore} represent capacitance of the porous layer and the electrolyte resistance inside the pores[56,61,67], respectively, while Q_{dl} and R_{ct} have the same physical meaning with that in Model D. The film capacitance under this condition is apparently higher than that listed in Supplementary Table 2, revealing that the oxide layer is degraded by high concentrations of fluoride.

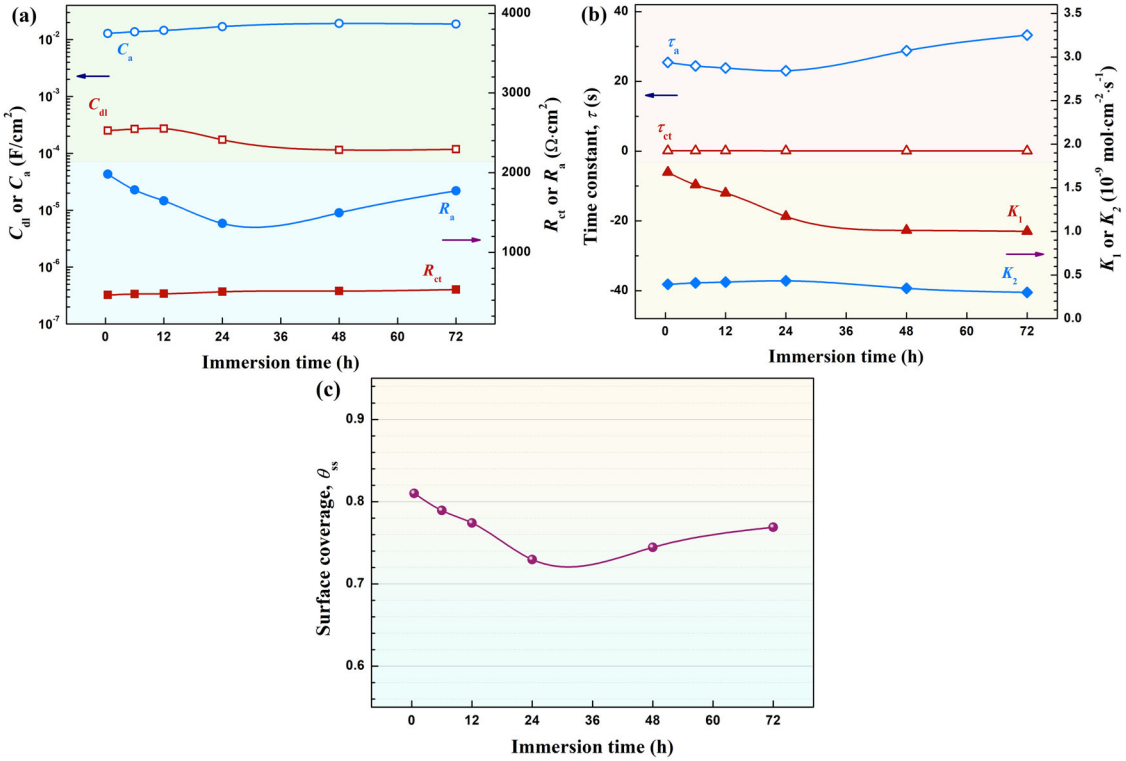

Fig. 10 EIS Fitting parameters in H_2SO_4 containing 0.002 M fluoride. a double layer and adsorption capacitance, **b** time constant and apparent rate constant, and **c** surface coverage.

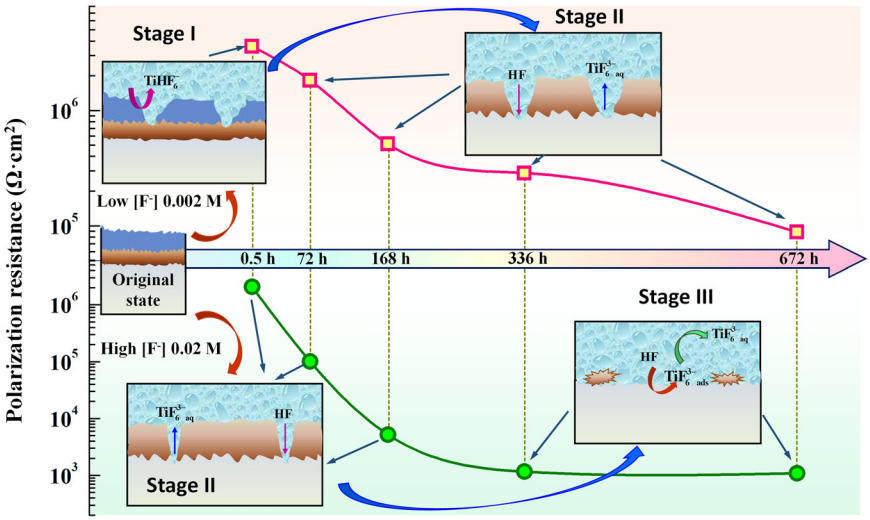

Fig. 11 Changes in polarization resistance and corresponding degradation stages of the thermally oxidized Ti (at 650 °C for 24 h). Surface state variations of the oxidized Ti in the presence of fluoride.

The EIS data during the long-term immersion test accompanied with the fitting results listed in Supplementary Table 5 clearly show the degradation process of the thermal oxide in the fluoride-containing environment. The degradation process is schematically illustrated in Fig. 11 in which the different interfacial structures and the fitted polarization resistances are presented. According to the EIS response, degradation of the protective oxide can be divided into three stages. Within Stage I, only the outer porous layer of the oxide is damaged, allowing the corrosive species to diffuse towards the inner layer and resulting in its dissolution. Even so, the Ti substrate is gracefully protected and the two time constants correspond to the bi-layer structure of the oxide film. The condition that the oxide is exposed in the dilute solution containing 0.002 M fluoride for 0.5 h belongs to this stage. When the immersion time exceeds 72 h or the fluoride concentration is increased to 0.02 M, corrosion enters the Stage II during which only one time constant that induced by surface oxide can be recognized. The pronounced characteristic of this period is the detection of the well-defined high-frequency capacitive loop, suggesting the deterioration of the surface oxide and the occurrence of Ti dissolution at the oxide/metal interface. After immersion

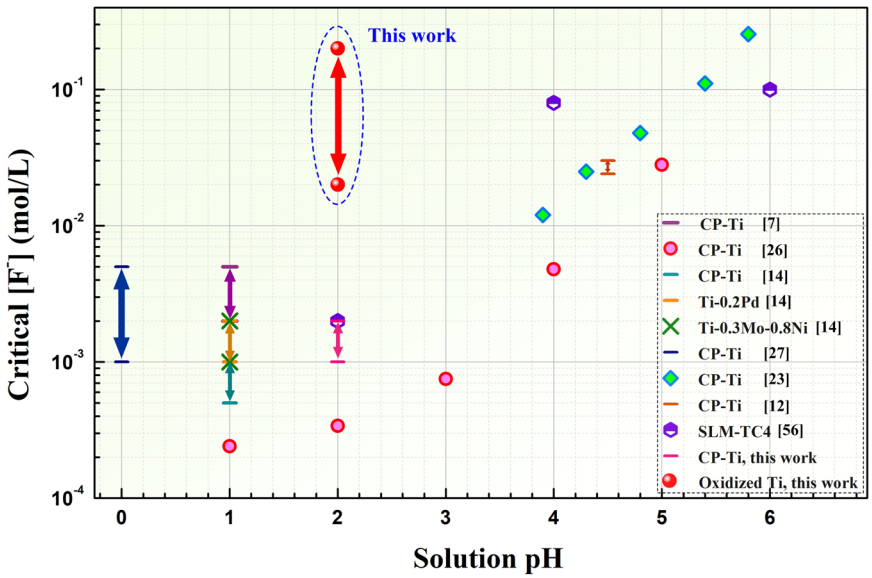

Fig. 12 Differences in critical [F⁻] between this work and the literature. Summary of the critical [F⁻] in the literature.

Table 2. Comparison of the critical fluoride concentration of pure Ti and its alloys in the literature with the present work.

Material	Electrolyte	pH	Temperature (°C)	Determination method	Critical [F⁻]	Ref.
CP-Ti	H_2SO_4	1.0	50	OCP, Pol, EIS	0.0005~0.002	7
CP-Ti	H_2SO_4	1.0	25	OCP, Pol	0.00024	26
CP-Ti	H_2SO_4	2.0	25	OCP, Pol	0.00034	
CP-Ti	H_2SO_4	3.0	25	OCP, Pol	0.00075	
CP-Ti	H_2SO_4	4.0	25	OCP, Pol	0.0048	
CP-Ti	H_2SO_4	5.0	25	OCP, Pol	0.028	
CP-Ti	H_2SO_4	1.0	25	OCP, Pol, EIS	0.0005~0.001	14
Ti-0.2 Pd	H_2SO_4	1.0	25	OCP, Pol, EIS	0.001~0.002	
Ti-0.3Mo-0.8Ni	H_2SO_4	1.0	25	OCP, Pol, EIS	0.001~0.002	
CP-Ti	$HClO_4$	0	22	OCP, EIS	0.001~0.005	27
CP-Ti	Artificial saliva	3.9	37	OCP, Pol	0.012	23
CP-Ti	Artificial saliva	4.3	37	OCP, Pol	0.025	
CP-Ti	Artificial saliva	4.8	37	OCP, Pol	0.048	
CP-Ti	Artificial saliva	5.4	37	OCP, Pol	0.111	
CP-Ti	Artificial saliva	5.8	37	OCP, Pol	0.255	
CP-Ti	Artificial saliva	4.5	37	OCP	0.024~0.03	12
SLM-Ti-6Al-4V	Artificial saliva	2.0	37	OCP	0.002	56
SLM-Ti-6Al-4V	Artificial saliva	4.0	37	OCP	0.08	
SLM-Ti-6Al-4V	Artificial saliva	6.0	37	OCP	0.1	
CP-Ti	H_2SO_4	2.0	25	Pol, EIS	0.001~0.002	This work
Oxidized CP-Ti	H_2SO_4	2.0	25	Pol, EIS	0.02~0.2	

in the solution containing 0.002 M fluoride for 672 h, corrosion of Ti still exists in the Stage II which indicates that the oxide formed at 650 °C for 24 h possesses the superior corrosion resistance in this environment. In the acidic environment containing 0.02 M fluoride, however, corrosion develops to the Stage III after the immersion time reaches 336 h during which the protective ability of the oxide is entirely annihilated. In this case, corrosion of the oxide-covered Ti exhibits the same characteristics with the pure Ti, which proceeds with the two consecutive steps and generates two well-discerned capacitive loops (Fig. 7c).

As proposed by Wang et al.[26], the critical fluoride concentration for corrosion of Ti was defined as the concentration where the maximum anodic current density (I_m) was equal to the cathodic current density ($|I_c|_{Em}$) at the critical potential (E_m) with the following equation:

$$I_m = |I_c|_{E_m} = \left|I_c^H\right| + \left|I_c^O\right| = I_{0,c}^H \exp\left(-\frac{E - E_{e,c}^H}{\beta_c}\right) + I_L^O \quad (10)$$

where $I_{0,c}^H$ is the exchange current density of hydrogen evolution reaction (HER), $E_{e,c}^H$ is the equilibrium potential of HER, I_L^O is the

limiting diffusion current density of oxygen reduction reaction, and β_c is the cathodic Tafel slope. In this case, the critical value can be intelligibly confirmed when detecting the transition of electrochemical response of Ti from the spontaneous passivation to the active-passive behavior. According to this diagnosis criterion, the critical fluoride concentrations of pure Ti in pH 2 solution is between 0.001 and 0.002 M, while that of the oxidized Ti (650 °C, 24 h) is increased to the range between 0.02 and 0.2 M. Table 2 lists the critical fluoride concentration of Ti-based materials in the fluoride-containing solutions with different pH in the literature[7,12,14,23,25–27,56] to allow the comparison with that of the oxidized Ti in the present work and the results are shown in Fig. 12. In H_2SO_4, Wang et al.[26] established the relationship between the critical fluoride concentration and pH within the pH range from 0 to 5 of pure Ti. Taking pH 2.0 as an example, the threshold value is 0.0034 M, which is far lower than that of oxidized Ti. In the artificial saliva, the increase of pH increases the critical fluoride concentration to values higher than 0.01 M[12,23], which is comparable with that of the oxidized Ti in acidic environment. When comparing with the titanium alloys including the Ti-0.2 Pd, Ti-0.3Mo-0.8Ni[14], and Ti6Al4V[56], the oxidized Ti also exhibits 1~2 orders magnitude higher critical fluoride concentration (Fig. 12), suggesting the high stability of the compact thermal oxide (TiO_2) in the fluoride-bearing acidic environments.

METHODS

Materials and electrolytes

Commercial pure Ti (CP-Ti, Grade 2, with $N \le 0.03$, $C \le 0.08$, Fe ≤ 0.20, $O \le 0.15$ in wt.) was used as the substrate material with the dimensions of $20 \times 20 \times 3$ cm^3, which was ground consecutively to 1500 # abrasive paper, degreased with ethanol, and dried in air before oxidation. The thermal oxidation was conducted in a muffle furnace under ambient atmosphere and the thermodynamic process was shown in Supplementary Fig. 5 (*supporting information*). After putting the samples inside the furnace, the temperature was increased to the designed values with a rate of 10 °C/min. Then the samples were kept at 500, 650, and 800 °C for 2 or 24 h to generate the thermal oxide film. After that, the samples were cooled with the furnace to 200 °C and then were took out from the furnace to an air cooling.

Table 3. Chemical composition of the simulated condensates used in the present work.

Analytical grade reagent	H_2SO_4 (98%)	HCl (37%)	HNO_3 (68%)	NaF	pH
Concentration (mg/L)	514.6	715.1	73.2	95.9	2.0

The testing electrolyte was the simulated condensates in a serving chimney of a thermal power plant in China[5], of which the chemical composition was listed in Table 3. The contents of the species were based on the analytical results of the real condensates collected in the chimney. Analytical grade reagents including the H_2SO_4 (98%, CAS number 7664-93-9), HCl (35%, CAS number 7647-01-0), HNO_3 (68%, CAS number 7697-37-2), NaF (CAS number 7681-49-4), and ultra-pure water (18.2 MΩ·cm) were used to prepare the solution and H_2SO_4 was used to adjust the pH to 2.0. All the reagents are provided by Sinopharm Chemical Reagent Co., Ltd. To investigate the effect of fluoride concentration on the corrosion behavior, the H_2SO_4 (pH = 2.0) containing different concentrations of fluorides was also used and the research purposes were listed in Table 4.

Microstructural, composition, and hardness characterization

Surface morphologies of the thermal oxides were observed by scanning electron microscope (SEM, Quanta 250) with a voltage of 20 kV, working distance of 10 mm, and beam current of 150 μA, using the secondary electron mode. To characterize the cross-sectional morphologies, the oxidized samples were mounted in the epoxy resin, exposing one cross-sectional surface, which was ground and polished sequentially to create a clean and smooth surface. A thin gold layer was sprayed on the cross-sectional surface to increase the conductivity of the resin and reduce the charge effect. The measurement parameters were the same to that used in surface morphologies, but the backscattered electron mode was used to clarify the interface area. Surface topography and nanoscale structures of the oxide film formed after 24 h were detected by an atomic force microscope (AFM, Bruker Multimode VIII) in ScanAsyst-air mode. The film roughness and the typical linear profiles were obtained.

Composition of the surface film was identified by wide-angle X-ray diffraction (XRD, Rigaku Dmax-rc) with the following parameters: voltage 40 kV, current 40 mA, Cu-Kα target, X-ray wavelength 0.15406 nm, scanning range 20° to 70°, and scanning step 2°/min. It was also characterized by XPS with ESCLAB 250Xi analyzer. The monochromatic Al-Kα X-ray source with a spot size of 400 μm was used and the survey spectra were recorded at a pass energy of 50 eV and a step size of 1.0 eV. High-resolution spectra of Ti 2p, O 1 s, and C 1 s core levels were recorded at a pass energy of 20 eV and a step size of 0.1 eV. All the XPS peaks were corrected to standard carbon C 1 s binding energy of 285 eV. Microhardness of the untreated and the thermally oxidized CP-Ti was performed on the Vickers harness tester (JMHVS-1000ZCCD) with applying 50 g load for 10 s. Five indentations were produced on each sample and the average values were calculated.

Electrochemical measurements

Specimens used in the electrochemical testing were the as-received Ti ($10 \times 10 \times 3$ cm^3) and the oxidized Ti ($20 \times 20 \times 3$ cm^3), leaving the exposure surface of 1 cm^2 to contact with the electrolytes. The measurements were performed with a conventional three-electrode cell, using saturated calomel electrode (SCE) as the reference electrode and the platinum plate as the counter electrode. Open circuit potential (OCP) and potentiodynamic polarization curves were conducted on the CHI660 electrochemical workstation. The former was recorded during

Table 4. Detailed approach, electrolyte, immersion time, and research purpose of the electrochemical measurements.

Materials	Electrolytes	Method	Time	Purpose
As-received and oxidized Ti under different conditions	Simulated condensates	OCP, Pol, EIS	Stabilization for 1 h	Clarify the effect of oxide film on the corrosion behavior and determine the optimum processing parameter.
As-received Ti	H_2SO_4 (pH = 2) [F^-] = 0, 0.0005, 0.001, 0.002 M	Pol, EIS	Stabilization for 0.5 h	Clarify the effect of [F^-] on the corrosion of bare Ti and determine the critical [F^-].
Oxidized Ti at 650 °C for 24 h	H_2SO_4 (pH = 2) [F^-] = 0.002, 0.02, 0. 2 mol/L	Pol, EIS	Stabilization for 0.5 h	Clarify the effect of [F^-] on the corrosion of oxidized Ti and determine the critical [F^-].
As-received Ti	H_2SO_4 (pH = 2) [F^-] = 0.002 mol/L	EIS	0.5, 6, 12, 24, 48, 72 h	Clarify the corrosion mechanism of bare Ti in fluoride-containing environment.
Oxidized Ti at 650 °C for 24 h	H_2SO_4 (pH = 2) [F^-] = 0.002, 0.02 mol/L	EIS	0.5, 72, 168, 336, 672 h	Clarify the long-term degradation mechanism of oxidized Ti in fluoride-containing environment.

immersion of the oxidized samples for 1 h, while the latter were measured with a scan rate of 0.5 mV^s^{-1} starting from the cathodic direction to 2.0 V_{SCE}. Electrochemical impedance spectroscopy (EIS) was measured via the Zahner Zennium-E potentiostat within the frequency range from 100 kHz to 10 mHz by imposing a 10 mV amplitude sinusoidal voltage. A total of 56 data points were collected and each point was repeated for 4 times, while the data point number varied with the frequency decade from 11 data points within $10^5 \sim 10^4$ Hz to 5 data points within 10^{-1}~10^{-2} Hz. The spectra of pure Ti during long-term immersion were composed of 84 data points with 12 points per decade. The detailed measurement method, electrolyte, immersion time, and research purpose are listed in Table 4. All the electrochemical measurements were conducted at 25 ± 2 °C and were repeated at least for three times to check the reproducibility.

Corrosion morphology observation

To clearly present the corrosion resistance of the oxidized samples, corrosion morphologies of the untreated Ti and oxidized Ti at 650 °C for 24 h after immersion were observed by SEM. The samples were firstly immersed in H_2SO_4 solution (pH = 0 and 2) containing 0.002 M fluoride for 24 h at OCP. After that, the samples were retrieved from the solution, washed by distilled water, and degreased with ethanol. It should be noted that there was no need to removing the surface corrosion products because no attached scales were reserved. The secondary electron mode was used to capture the surface morphologies of the corroded samples and the parameters were the same to that used in microstructure observation.

DATA AVAILABILITY

The raw/processed data required to reproduce these findings can be obtained by sending an email to the corresponding author.

Received: 16 March 2022; Accepted: 15 July 2022;
Published online: 05 August 2022

REFERENCES

1. Shoemaker, L. & Crum, J. R. Experience in effective application of metallic materials for construction of FGD systems. *Special Metals* www.specialmetals.com (2010).
2. Shoemaker, L., Crum, J., Maitra, D., Muro, R. & Neighbor, M. *Recent Experience With Stainless Steels in FGD Air Pollution Control Service. Corrosion* 2011 (NACE International, 2011).
3. Zeng, Y., Li, K., Hughes, R. & Luo, J. L. Corrosion mechanisms and materials selection for the construction of flue gas component in advanced heat and power systems. *Ind. Eng. Chem. Res.* **56**, 14141–14154 (2017).
4. Pan, P., Chen, H., Liang, Z. & Zhao, Q. Desulfurized flue gas corrosion coupled with deposits in a heating boiler. *Corros. Sci.* **131**, 126–136 (2018).
5. Cui, Z. et al. Influence of temperature on the electrochemical and passivation behavior of 2507 super duplex stainless steel in simulated desulfurized flue gas condensates. *Corros. Sci.* **118**, 31–48 (2017).
6. Dou, Y., Han, S., Wang, L., Wang, X. & Cui, Z. Characterization of the passive properties of 254SMO stainless steel in simulated desulfurized flue gas condensates by electrochemical analysis, XPS and ToF-SIMS. *Corros. Sci.* **165**, 108405 (2020).
7. Wang, Z. B., Hu, H. X., Liu, C. B. & Zheng, Y. G. The effect of fluoride ions on the corrosion behavior of pure titanium in 0.05M sulfuric acid. *Electrochim. Acta* **135**, 526–535 (2014).
8. Bordzilowski, J. & Darowicki, K. Anti-corrosion protection of chimneys and flue gas ducts. *Anti-Corros. Method. Mater.* **45**, 388–396 (1998).
9. Li, X. et al. Understanding the effect of fluoride on corrosion behavior of pure titanium in different acids. *Corros. Sci.* **192**, 109812 (2021).
10. Stancheva, M. & Bojinov, M. Influence of fluoride content on the barrier layer formation and titanium dissolution in ethylene glycol–water electrolytes. *Electrochim. Acta* **78**, 65–74 (2012).
11. Amrutha, M. S., Fasmin, F. & Ramanathan, S. Effect of HF concentration on anodic dissolution of titanium. *J. Electrochem. Soc.* **164**, H188–H197 (2017).
12. Li, Y. & Xu, J. Is niobium more corrosion-resistant than commercially pure titanium in fluoride-containing artificial saliva? *Electrochim. Acta* **233**, 151–166 (2017).
13. Industrial, I. C. O. *Model Code for Steel Chimneys*. (CICIND, 1999).
14. Wang, Z. B., Hu, H. X., Zheng, Y. G., Ke, W. & Qiao, Y. X. Comparison of the corrosion behavior of pure titanium and its alloys in fluoride-containing sulfuric acid. *Corros. Sci.* **103**, 50–65 (2016).
15. Cui, Z. et al. Electrochemical behavior and surface characteristics of pure titanium during corrosion in simulated desulfurized flue gas condensates. *J. Electrochem. Soc.* **165**, C542–C561 (2018).
16. Kumar, S., Narayanan, T. S. N. S., Raman, S. G. S. & Seshadri, S. K. Thermal oxidation of CP Ti—An electrochemical and structural characterization. *Mater. Charact.* **61**, 589–597 (2010).
17. Shankar, A. R., Karthiselva, N. S. & Mudali, U. K. Thermal oxidation of titanium to improve corrosion resistance in boiling nitric acid medium. *Surf. Coat. Technol.* **235**, 45–53 (2013).
18. Wang, S., Liao, Z., Liu, Y. & Liu, W. Influence of thermal oxidation temperature on the microstructural and tribological behavior of Ti6Al4V alloy. *Surf. Coat. Technol.* **240**, 470–477 (2014).
19. Zhang, Y., Ma, G.-R., Zhang, X.-C., Li, S. & Tu, S.-T. Thermal oxidation of Ti-6Al–4V alloy and pure titanium under external bending strain: Experiment and modelling. *Corros. Sci.* **122**, 61–73 (2017).
20. Ashrafizadeh, A. & Ashrafizadeh, F. Structural features and corrosion analysis of thermally oxidized titanium. *J. Alloy. Compd.* **480**, 849–852 (2009).
21. Kumar, S., Narayanan, T. S., Raman, S. G. S. & Seshadri, S. Thermal oxidation of CP-Ti: evaluation of characteristics and corrosion resistance as a function of treatment time. *Mater. Sci. Eng. C.* **29**, 1942–1949 (2009).
22. Birch, J. & Burleigh, T. Oxides formed on titanium by polishing, etching, anodizing, or thermal oxidizing. *Corrosion* **56**, 1233–1241 (2000).
23. Nakagawa, M., Matsuya, S., Shiraishi, T. & Ohta, M. Effect of fluoride concentration and pH on corrosion behavior of titanium for dental use. *J. Dent. Res.* **78**, 1568–1572 (1999).
24. Huang, H.-H. Electrochemical impedance spectroscopy study of strained titanium in fluoride media. *Electrochim. Acta* **47**, 2311–2318 (2002).
25. Kong, D.-S. & Feng, Y.-Y. Electrochemical anodic dissolution kinetics of titanium in fluoride-containing perchloric acid solutions at open-circuit potentials. *J. Electrochem. Soc.* **156**, C283–C291 (2009).
26. Wang, Z. B., Hu, H. X. & Zheng, Y. G. Determination and explanation of the pH-related critical fluoride concentration of pure titanium in acidic solutions using electrochemical methods. *Electrochim. Acta* **170**, 300–310 (2015).
27. Fovet, Y., Gal, J.-Y. & Toumelin-Chemla, F. Influence of pH and fluoride concentration on titanium passivating layer: stability of titanium dioxide. *Talanta* **53**, 1053–1063 (2001).
28. Mareci, D. et al. Effect of acidic fluoride solution on the corrosion resistance of ZrTi alloys for dental implant application. *Corros. Sci.* **87**, 334–343 (2014).
29. Kumar, S., Sankara Narayanan, T. S. N., Ganesh Sundara Raman, S. & Seshadri, S. K. Fretting corrosion behaviour of thermally oxidized CP-Ti in Ringer's solution. *Corros. Sci.* **52**, 711–721 (2010).
30. Tkachenko, S. et al. Isothermal oxidation behavior of experimental Ti−Al−Si alloys at 700 °C in air. *J. Alloy. Compd.* **694**, 1098–1108 (2017).
31. Yan, H.-J., Tai, Z.-F., Wu, L.-K. & Cao, F.-H. Improved high-temperature oxidation resistance of TC4 alloy by electrodeposited SiO_2 coating. *Corros. Commun.* **3**, 34–44 (2021).
32. Leonardi, S. et al. TiO_2 Nanotubes: Interdependence of substrate grain orientation and growth rate. *ACS Appl. Mater. Interfaces* **7**, 1662–1668 (2015).
33. Ebrahimi, A. R., Zarei, F. & Khosroshahi, R. A. Effect of thermal oxidation process on fatigue behavior of Ti-4Al-2V alloy. *Surf. Coat. Technol.* **203**, 199–203 (2008).
34. Ningshen, S., Sakairi, M., Suzuki, K. & Okuno, T. Corrosion performance and surface analysis of Ti–Ni–Pd–Ru–Cr alloy in nitric acid solution. *Corros. Sci.* **91**, 120–128 (2015).
35. Steven, Y. Y., Scully, J. R. & Vitus, C. M. Influence of niobium and zirconium alloying additions on the anodic dissolution behavior of activated titanium in HCl solutions. *J. Electrochem. Soc.* **148**, B68 (2001).
36. Pan, H. et al. Effect of alloyed Sr on the microstructure and corrosion behavior of biodegradable Mg-Zn-Mn alloy in Hanks' solution. *Corros. Sci.* **157**, 420–437 (2019).
37. Mazare, A. et al. Corrosion, antibacterial activity and haemocompatibility of TiO_2 nanotubes as a function of their annealing temperature. *Corros. Sci.* **103**, 215–222 (2016).
38. Krishna, N. G., George, R. P. & Philip, J. Anomalous enhancement of corrosion resistance and antibacterial property of commercially pure Titanium (CP-Ti) with nanoscale rutile titania film. *Corros. Sci.* **172**, 108678 (2020).
39. Lyapin, A., Jeurgens, L. P. H. & Mittemeijer, E. J. Effect of temperature on the initial, thermal oxidation of zirconium. *Acta Mater.* **53**, 2925–2935 (2005).
40. Wen, M., Wen, C., Hodgson, P. & Li, Y. Improvement of the biomedical properties of titanium using SMAT and thermal oxidation. *Colloids Surf. B Biointerfaces* **116**, 658–665 (2014).
41. Padma, R., Ramkumar, K. & Satyam, M. Growth of titanium oxide overlayers by thermal oxidation of titanium. *J. Mater. Sci.* **23**, 1591–1597 (1988).

42. Istrate, B. et al. Influence of time on thermal oxidation of CP-Ti grade II at 850 °C. *Key Eng. Mater.* **614**, 35–40 (2014).
43. Kofstad, P. High-temperature oxidation of titanium. *J. Common Met.* **12**, 449–464 (1967).
44. Kumar, S., Sankara Narayanan, T. S. N., Ganesh Sundara Raman, S. & Seshadri, S. K. Thermal oxidation of Ti6Al4V alloy: Microstructural and electrochemical characterization. *Mater. Chem. Phys.* **119**, 337–346 (2010).
45. Jamesh, M., Sankara Narayanan, T. S. N. & Chu, P. K. Thermal oxidation of titanium: Evaluation of corrosion resistance as a function of cooling rate. *Mater. Chem. Phys.* **138**, 565–572 (2013).
46. Güleryüz, H. & Çimenoğlu, H. Effect of thermal oxidation on corrosion and corrosion–wear behaviour of a Ti–6Al–4V alloy. *Biomaterials* **25**, 3325–3333 (2004).
47. Barranco, V., Onofre, E., Escudero, M. L. & García-Alonso, M. C. Characterization of roughness and pitting corrosion of surfaces modified by blasting and thermal oxidation. *Surf. Coat. Technol.* **204**, 3783–3793 (2010).
48. Wang, S., Liao, Z., Liu, Y. & Liu, W. Influence of thermal oxidation duration on the microstructure and fretting wear behavior of Ti6Al4V alloy. *Mater. Chem. Phys.* **159**, 139–151 (2015).
49. Sun, Q., Hu, T., Fan, H., Zhang, Y. & Hu, L. Thermal oxidation behavior and tribological properties of textured TC4 surface: Influence of thermal oxidation temperature and time. *Tribol. Int.* **94**, 479–489 (2016).
50. Hsu, C. H. & Mansfeld, F. Concerning the conversion of the constant phase element parameter Y_0 into a capacitance. *Corrosion* **57**, 747–748 (2001).
51. Brug, G., van den Eeden, A. L., Sluyters-Rehbach, M. & Sluyters, J. H. The analysis of electrode impedances complicated by the presence of a constant phase element. *J. Electroanal. Chem.* **176**, 275–295 (1984).
52. Alves, V. A. et al. In situ impedance spectroscopy study of the electrochemical corrosion of Ti and Ti–6Al–4V in simulated body fluid at 25 °C and 37 °C. *Corros. Sci.* **51**, 2473–2482 (2009).
53. Gai, X. et al. Electrochemical behaviour of passive film formed on the surface of Ti-6Al-4V alloys fabricated by electron beam melting. *Corros. Sci.* **145**, 80–89 (2018).
54. Kolasinski, K. W. The composition of fluoride solutions. *J. Electrochem. Soc.* **152**, J99 (2005).
55. Robin, A. & Meirelis, J. P. Influence of fluoride concentration and pH on corrosion behavior of titanium in artificial saliva. *J. Appl. Electrochem.* **37**, 511–517 (2007).
56. Zhang, H. et al. The corrosion behavior of Ti6Al4V fabricated by selective laser melting in the artificial saliva with different fluoride concentrations and pH values. *Corros. Sci.* https://doi.org/10.1016/j.corsci.2020.109097 (2020).
57. Orazem, M. E. & Tribollet, B. *Electrochemical Impedance Spectroscopy* (John Wiley & Sons, 2011).
58. Tang, J. et al. The effect of H_2S concentration on the corrosion behavior of carbon steel at 90 °C. *Corros. Sci.* **52**, 2050–2058 (2010).
59. Cheng, X., Ma, H., Chen, S., Chen, X. & Yao, Z. Corrosion of nickel in acid solutions with hydrogen sulphide. *Corros. Sci.* **42**, 299–311 (2000).
60. Hernández-López, J. M., Conde, A., de Damborenea, J. J. & Arenas, M. A. Electrochemical response of TiO_2 anodic layers fabricated on Ti6Al4V alloy with nanoporous, dual and nanotubular morphology. *Corros. Sci.* **112**, 194–203 (2016).
61. Alves, A. C. et al. Corrosion mechanisms in titanium oxide-based films produced by anodic treatment. *Electrochim. Acta* **234**, 16–27 (2017).
62. Pan, J., Thierry, D. & Leygraf, C. Electrochemical impedance spectroscopy study of the passive oxide film on titanium for implant application. *Electrochim. Acta* **41**, 1143–1153 (1996).
63. Calderon Moreno, J. M. et al. Surface and electrochemical characterization of a new ternary titanium based alloy behaviour in electrolytes of varying pH. *Corros. Sci.* **77**, 52–63 (2013).
64. Ćurković, L., Ćurković, H. O., Salopek, S., Renjo, M. M. & Šegota, S. Enhancement of corrosion protection of AISI 304 stainless steel by nanostructured sol–gel TiO_2 films. *Corros. Sci.* **77**, 176–184 (2013).
65. Cui, Z., Li, X., Xiao, K. & Dong, C. Atmospheric corrosion of field-exposed AZ31 magnesium in a tropical marine environment. *Corros. Sci.* **76**, 243–256 (2013).
66. Duarte, L. T., Biaggio, S. R., Rocha-Filho, R. C. & Bocchi, N. Surface characterization of oxides grown on the Ti–13Nb–13Zr alloy and their corrosion protection. *Corros. Sci.* **72**, 35–40 (2013).
67. Zhang, H. et al. Different corrosion behaviors between α and β phases of Ti6Al4V in fluoride-containing solutions: Influence of alloying element Al. *Corros. Sci.* **169**, 108605 (2020).

ACKNOWLEDGEMENTS

The authors wish to acknowledge the financial support of National Natural Science Foundation of China (Nos. 51701102 and 51931008).

AUTHOR CONTRIBUTIONS

L. W.: investigation, writing—original draft; M. W.: investigation; M. Z.: investigation, visualization; X. L.: investigation, visualization; Z. C.: investigation, writing—review and editing, supervision, funding acquisition.

COMPETING INTERESTS

The authors declare no competing interests.

ADDITIONAL INFORMATION

Supplementary information The online version contains supplementary material available at https://doi.org/10.1038/s41529-022-00275-9.

Correspondence and requests for materials should be addressed to Zhongyu Cui.

Reprints and permission information is available at http://www.nature.com/reprints

Publisher's note Springer Nature remains neutral with regard to jurisdictional claims in published maps and institutional affiliations.